Effect of C_{3v} symmetry breaking on the noncentrosymmetric quantum spin Hall insulating phase and optical characteristics of monolayer PbBiI

Bui D. Hoi ●*

Department of Physics and Center for Theoretical and Computational Physics, University of Education,
Hue University, Hue 530000, Viet Nam

Due to the rise of applications in several optoelectronic and spintronic platforms, theoretically engineering the propagation of light in low-dimensional systems dealing with both charge and spin degrees of freedom has recently triggered considerable interest. By breaking the C_{3v} symmetry through external exchange fields, we engineer the propagation of an incident circularly polarized light in a noncentrosymmetric quantum spin Hall insulator, monolayer PbBiI, that is active in the near-infrared region of the electromagnetic spectrum. The Kubo formalism is ideal for optical properties. We endeavor to thoroughly demonstrate that a critical-breaking regime of three types of fields leads to various anisotropic electronic phases and optical interband transitions. We find various near-to-far infrared shifts for the optical activity of the system when the C_{3v} symmetry breaking fields are turned on. This is proven in the ensuing two ways: The spectrum of optical conductivity components and the intensities of scattered/absorbed light. We further find the criteria under which the system is transparent. Finally, depending on the exchange fields, we engineer the eccentricities for the reflected and transmitted lights in monolayer PbBiI to see how the polarization of incident circular light becomes linear and elliptical. The applicability of results in industry and medicine is also briefly discussed.

I. INTRODUCTION

The discovery of the integer quantum Hall effect is the onset of topology in solid-state physics [1,2]. Also, the discovery of graphene as the first two-dimensional (2D) material [3–5] is the birth of 2D topological insulators with unique properties of inherent spin-orbit coupling (SOC) and band inversion [6–9]. These systems are called quantum spin Hall insulators (QSHIs) due to their bulk states in two dimensions which indicate an insulating gapped phase and their surface states which appear with a semimetallic fully spin-polarized gapless phase associated with helical edge modes. The time-reversal symmetry is responsible for the protection of surface states. QSHIs with novel quantum states are a major step forward in materials science and more importantly in potential applications for spintronics and topological quantum computation [10–12]. An extrinsic SOC term of Rashba type also exists when the inversion symmetry between spin-dependent surface states is broken, leading to opposite in-plane chiral spin textures in the band dispersion [11]. This coupling can be induced into the system by a built-in electric field and it can tune the spin direction in QSHIs [13–15].

To date, various types of materials formed by heavy elements with strong intrinsic and extrinsic Rashba SOCs such as Bi, Pb, and W are found [16–20]. Among others, it has been recently reported that noncentrosymmetric QSHIs (NCS-QSHIs) formed by honeycomb lattices of IV, V, and VII elements [21] pose the simultaneous presence of both

Rashba and band inversion, resulting in a Rashba-like SOC and an unconventional spin texture. In contrast to most doped QSHIs, this type is associated with time-reversal symmetry protection for both the edge and bulk states. This feature leads to less energy loss in the system since the bulk backscattering is forbidden. Thus the integration of topological states in these materials is much easier and accordingly, a proper spintronic device can be constructed. Various extensive methods have been proposed to tune the physical properties of QSHIs. For example, it has been reported that the inelastic backscattering and quantum phases in these systems can be influenced by the electron-electron interaction [22–28]. A bias voltage can produce a spin polarization in the equilibrium state of these phases [6,29,30]. An external magnetic field can also affect the electronic and transport properties of QSHIs [31–35], etc.

In NCS-QSHIs, the IV-V elements form a honeycomb lattice which is weakly stacked with VII elements [21,36–38]. The PbBiI compound (Bi = V, Pb = IV, and I = VII) is an alternating candidate for the coexistence of both Rashba-like splitting and band inversion. To confirm that PbBiI is a QSHI, it has been checked that the evolution of the Wannier center of charges can not be crossed an odd number of times [21]. In the PbBiI system, the time-reversal symmetry is preserved and band inversion at the Γ point originates from the SOC. The buckled format of these stable noncentrosymmetric systems obeys the C_{3v} symmetry that is comprised of three operators: (i) time-reversal symmetry $\mathcal{T}$, (ii) threefold rotation symmetry $\mathcal{R}_3$ along the z axis, and (iii) the mirror symmetry $\mathcal{M}_x$ in the y-z plane.

The by now presented works on these systems have provided a quite profound understanding of how an external field
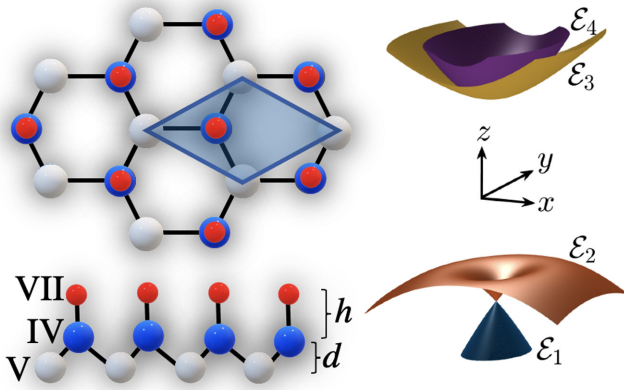
*buidinhhoi@hueuni.edu.vn

FIG. 1. (Left) Top and side views of the lattice geometry for monolayer PbBiI with Bi = V, Pb = IV, and I = VII elements. The buckled parameter is $d \simeq 1.3$ Å, while bond lengths of Pb-I (h) and Bi-Pb are respectively 1.35 and 3.04 Å. (Right) The isotropic electronic band structure of pristine monolayer PbBiI consisting of four bands $\mathcal{E}_1$, $\mathcal{E}_2$, $\mathcal{E}_3$, and $\mathcal{E}_4$ respectively from basis $|Bi_{1/2}, +1/2\rangle$, $|Bi_{1/2}, -1/2\rangle$, $|Bi_{3/2}, +1/2\rangle$, and $|Bi_{3/2}, -1/2\rangle$.

brings novel physical insights into the system. It furthermore asserts, the eventually reached insights can generally lead to amazing electronic and spintronic transport properties. However, much less attention is paid to an efficient powerful C_{3v} symmetry breaking (CSB) protocol about the band engineering of NCS-QSHIs based on which the optical properties can also be controlled. And even scarcer are general predictions describing the competition between the type of CSB field in tuning the band dispersion. The PbBiI compound is optically active in the near-infrared region of electromagnetic spectrum. In this paper, we study the propagation of an incident near-infrared light in monolayer PbBiI under the influence of two different CSB fields. This problem of engineering the electronic and optical properties poses novel fascinating physics useful for industry, science, and medical applications. The interplay between the proposed fields, bulk, and Rashba-like states in controlling the optical reflection, transmission, and absorption of near-infrared light as well as in tuning the polarization of the incident light in monolayer PbBiI are the overarching theme of this paper.

This paper is organized as follows. In Sec. II, we introduce the Hamiltonian model of the system in the presence of various CSB fields. In Secs. III and IV, we then use the Kubo formula governing the direction-dependent optical properties with the aid of linear response theory. In Sec. V, we present the numerical results by focusing on the effect of the CSB fields on the behaviors of electronic band structure, optical conductivity in all directions, and the intensity/eccentricity of scattered light. Finally, we summarize our findings in Sec. VI.

II. MODEL AND THEORY

A. Pristine monolayer PbBiI

In the left side of Fig. 1, we start with a sketch of a honeycomb lattice of monolayer PbBiI with Bi = V, Pb = IV, and I = VII elements. The buckling parameter is given

by $d \simeq 1.3$ Å and the bond lengths between elements are 1.35 and 3.04 Å for Pb-I (h) and Bi-Pb dimers, respectively. The *ab initio* calculations [21,39–41] have presented that the highest valence band is mainly originated from the $p_{x,y}$-Bi orbitals, while the lowest conduction band is mainly formed by p_z-Bi orbitals. Thus the contribution of Pb-I dimers in determining the effective electronic band structure of PbBiI is negligible. Considering the spin degree of freedom of $S = 1/2$ and the p-orbital angular momentum of $L = 1$ for dominated Bi atoms in monolayer PbBiI, one can obtain the total angular momentum of $J = \{1/2, 3/2\}$ for both spin directions $j_z = \{+1/2, -1/2\}$. Hence, we continue with the SOC basis of Bi atoms $|J, j_z\rangle$.

Building on these, the total low-energy Hamiltonian of monolayer PbBiI in the vicinity of the Γ point constitutes four elements within the tight-binding approximation [21]:

$$\mathcal{H}_{\vec{k}} = \begin{pmatrix} -\varepsilon_{1/2} & 0 & 0 & 0 \\ 0 & -\varepsilon_{1/2} & 0 & 0 \\ 0 & 0 & +\varepsilon_{3/2} & 0 \\ 0 & 0 & 0 & +\varepsilon_{3/2} \end{pmatrix}$$
$$+ \begin{pmatrix} \zeta_{1/2}k^2 & i\alpha_{R,1/2}k_- & 0 & \gamma k_- \\ -i\alpha_{R,1/2}k_+ & \zeta_{1/2}k^2 & \gamma k_+ & 0 \\ 0 & \gamma k_- & -\zeta_{3/2}k^2 & 0 \\ \gamma k_+ & 0 & 0 & -\zeta_{3/2}k^2 \end{pmatrix},$$
(1)

where $k_\pm = k_x \pm ik_y$ and $k = \sqrt{k_x^2 + k_y^2}$ are momenta and the constants $\varepsilon_{1/2}$, $\varepsilon_{3/2}$, $\zeta_{1/2}$, $\zeta_{3/2}$, $\alpha_{R,1/2}$, and γ are the model parameters obtained from the phenomenological analysis of the electronic structure in the *ab initio* calculations [21]: $\varepsilon_{1/2} = 0.1685$ eV, $\varepsilon_{3/2} = 0.1575$ eV, $\zeta_{1/2} = 0.008187$ eV/Å^2, $\zeta_{3/2} = 0.038068$ eV/Å^2, $\alpha_{R,1/2} = 3.0919$ eV/Å, and $\gamma = -3.5853$ eV/Å. A brief comparison between the PbBiI Hamiltonian model and the Kane-Mele model is based on the lack of nearest-neighbor hopping terms. In other words, the Pb-I dimer in this model only mediates the interaction between Bi atoms through the next nearest neighbor hopping terms. Note that the warping effect due to the $\alpha_{R,3/2} \simeq 0$ is neglected throughout the present study.

The energy dispersion for this model has the form

$$\mathcal{E}_{\vec{k},v}^\tau = \tfrac{1}{2}[v\alpha_{R,1/2}k + \varepsilon + \zeta k^2 + \tau \mathcal{G}_v(\vec{k})], \quad (2a)$$

$$\mathcal{G}_v(\vec{k}) = \sqrt{\mathcal{C}k^2 + (\tilde{\varepsilon} - \tilde{\zeta}k^2)(-2v\alpha_{R,1/2}k + \tilde{\varepsilon} - \tilde{\zeta}k^2)}. \quad (2b)$$

Here $\varepsilon = \varepsilon_{3/2} - \varepsilon_{1/2}$, $\zeta = \zeta_{1/2} - \zeta_{3/2}$, $\tilde{\varepsilon} = \varepsilon_{3/2} + \varepsilon_{1/2}$, $\tilde{\zeta} = \zeta_{1/2} + \zeta_{3/2}$, and $\mathcal{C} = 4\gamma^2 + \alpha_{R,1/2}^2$. Also, $v = \pm 1$ shows the total angular momentum $J = 3/2$ ($v = +1$) and $J = 1/2$ ($v = -1$), while $\tau = \pm 1$ shows the spin direction $j_z = -1/2$ ($\tau = +1$) and $j_z = +1/2$ ($\tau = -1$). In the pristine state, the electronic band structure is isotropic in terms of the momentum $\vec{k}$ so close to the Γ point of the first Brillouin zone and consists of four bands $\mathcal{E}_1 = \mathcal{E}_{\vec{k},-1}^{-1}$, $\mathcal{E}_2 = \mathcal{E}_{\vec{k},-1}^{+1}$, $\mathcal{E}_3 = \mathcal{E}_{\vec{k},+1}^{-1}$, and $\mathcal{E}_4 = \mathcal{E}_{\vec{k},+1}^{+1}$, respectively, for basis $|1/2, +1/2\rangle$, $|1/2, -1/2\rangle$, $|3/2, +1/2\rangle$, and $|3/2, -1/2\rangle$. The bulk gap characterizing the band inversion originates from the bands close to the zero energy at zero ($\mathcal{E}_3$) and nonzero ($\mathcal{E}_2$) momenta, i.e., $\mathcal{E}_3 - \mathcal{E}_2 \simeq 0.275$ eV, while the Rashba-like spin splitting gap originates

from the bands in the valence side at zero ($\mathcal{E}_1$) and nonzero ($\mathcal{E}_2$) momenta, i.e., $\mathcal{E}_2 - \mathcal{E}_1 \simeq 0.051$ eV. This band structure is in excellent agreement with Ref. [21].

In the case of C_{3v} symmetry which is included in the band structure, we have

(i) $\mathcal{T}$: $|J, j_z\rangle \mapsto 2j_z \langle J, j_z|$,

(ii) $\mathcal{R}_3$: $|J, j_z\rangle \mapsto e^{2\mathrm{i} j_z \pi/3} |J, j_z\rangle$,

(iii) $\mathcal{M}_x$: $|J, j_z\rangle \mapsto -\mathrm{i} |J, j_z\rangle$.

To comprehensively look at the symmetries of the system shown in Fig. 1, we turn to the band structure of monolayer PbBiI in the right panel of Fig. 1. Far from the Γ point, the $\mathcal{R}_3$ threefold rotation symmetry along the z axis generates non-linear terms in the SOC such as the three-order Rashba term, resulting in the hexagonal warping effect in the bulk states. However, the warping effect due to the found $\alpha_{R,3/2} \simeq 0$ is neglected in the Hamiltonian. On the one hand, the only contribution coming from the lack of inversion symmetry is the first-order Rashba term including $\alpha_{R,1/2}$, covering the mirror symmetry $\mathcal{M}_x$. On the other hand, the time-reversal symmetry supports the Γ point itself. From these points, the only available symmetries in the C_{3v} symmetry of our Hamiltonian are $\mathcal{T}$ and $\mathcal{M}_x$. By these, we mean that the C_{3v} symmetry breaking here stems from the first-order Rashba term.

B. CSB-induced monolayer PbBiI

Now, we turn to define the physical CSB fields. We consider two types of fields here to tune the electronic phase and optical interband transitions. First, we apply an in-plane magnetization field $\mathcal{H}_{\mathrm{M}} = \mathcal{F}_{\mathrm{M}} \tau_0 \otimes \sigma_x$ to affect the orbital hybridization of the system, characterized by the Bi orbitals with opposite spin directions $j_z = \{+1/2, -1/2\}$. Second, we apply an inversion symmetry breaking (ISB) potential between the total angular momenta $J = \{1/2, 3/2\}$ by a field $\mathcal{H}_{\mathrm{ISB}} = \mathcal{F}_{\mathrm{ISB}} \tau_x \otimes \sigma_x$ to induce two different gauge shifts [42]. In these terms, τ_0 (τ_x) refers to the identity matrix (Pauli x matrix) of total angular momentum space, and σ_x is the Pauli x matrix of spin space. These fields are both invariant under the time-reversal symmetry, but another available symmetry $\mathcal{M}_x$ in the C_{3v} symmetry of PbBiI lattice is broken. Working with both fields together is also possible. Thus let us propose the following effective CSB-induced Hamiltonians as

$$\mathcal{H}_{\mathrm{M}}(\vec{k}) = \mathcal{H}(\vec{k}) + \mathcal{F}_{\mathrm{M}} \tau_0 \otimes \sigma_x, \tag{3a}$$

$$\mathcal{H}_{\mathrm{ISB}}(\vec{k}) = \mathcal{H}(\vec{k}) + \mathcal{F}_{\mathrm{ISB}} \tau_x \otimes \sigma_x, \tag{3b}$$

$$\mathcal{H}_{\mathcal{F}}(\vec{k}) = \mathcal{H}(\vec{k}) + \mathcal{F} J_2 \otimes \sigma_x, \tag{3c}$$

where in the last term we consider both fields together including $J_2 = \tau_0 + \tau_x$ as the unit matrix. It should be noted that $\mathcal{H}_{\mathrm{M/ISB}/\mathcal{F}} \mathcal{H}_{\vec{k}} \mathcal{H}_{\mathrm{M/ISB}/\mathcal{F}}^{-1} \neq \mathcal{H}_{\vec{k}}$, i.e., C_{3v} symmetry breaking occurs. Practically, there are possible methods to induce such CSB fields. For instance, in the magnetic proximity effect, magnetic exchange fields can be induced in a material by proximity to a ferromagnetic/antiferromagnetic substrate. These fields act on the orbital angular momentum in the basis of orbitals modifying the corresponding Hamiltonians. This method has been used recently for monolayer $MoTe_2$ nanoribbons on EuO substrate [43] and graphene on various substrates [44].

III. OPTICAL CONDUCTIVITY OF MONOLAYER PBBII

Considering the anisotropic electronic band structure of monolayer PbBiI in the presence of the CSB field, we turn to calculate the optical conductivity components $\sigma_{\alpha\beta}(\omega)$ of the material along different directions $\{\alpha, \beta\} = \{x, y\}$ when it is subjected to a light with energy $\hbar\omega$. In doing so, using the Hamiltonians in Eqs. (1) and (3), we invoke the Kubo formula and the linear response theory given by [45,46]

$$\sigma_{\alpha\beta}(\omega) = \mathrm{i} \sum_{\vec{k}} \sum_{\nu\nu'\eta\eta'} \frac{f_{\vec{k},\nu}^{\eta} - f_{\vec{k},\nu'}^{\eta'}}{\mathcal{E}_{\vec{k},\nu}^{\eta} - \mathcal{E}_{\vec{k},\nu'}^{\eta'}} \frac{\mathcal{J}_{\alpha\beta;\nu\nu'}^{\eta\eta'}(\vec{k})}{\hbar\omega + \mathrm{i}\delta + \mathcal{E}_{\vec{k},\nu}^{\eta} - \mathcal{E}_{\vec{k},\nu'}^{\eta'}}, \tag{4}$$

where

$$\mathcal{J}_{\alpha\beta;\nu\nu'}^{\eta\eta'}(\vec{k}) = \langle \vec{k}; \nu, \eta | j_\alpha | \vec{k}; \nu', \eta' \rangle \langle \vec{k}; \nu', \eta' | j_\beta | \vec{k}; \nu, \eta \rangle. \tag{5}$$

The term $f_{\vec{k},\nu}^{\eta} = 1/\exp([\mathcal{E}_{\vec{k},\nu}^{\eta} - \mu]/k_{\mathrm{B}}T) + 1]$ indicates the Fermi-Dirac distribution function at a given temperature T and chemical potential μ. In the denominator of Eq. (4), $\delta = 3$ meV is a small phenomenological broadening factor for controlling the width of optical peaks. The tensor quantity $\mathcal{J}_{\alpha\beta;\nu\nu'}^{\eta\eta'}(\vec{k})$ determines the correlation between currents along different directions, which can be given by the components of the current operator $j_\alpha = e\partial\mathcal{H}/\partial k_\alpha$:

$$j_x = e \begin{pmatrix} 2\zeta_{1/2}k_x & \mathrm{i}\alpha_{R,1/2} & 0 & \gamma \\ -\mathrm{i}\alpha_{R,1/2} & 2\zeta_{1/2}k_x & \gamma & 0 \\ 0 & \gamma & -2\zeta_{3/2}k_x & 0 \\ \gamma & 0 & 0 & -2\zeta_{3/2}k_x \end{pmatrix}, \tag{6a}$$

$$j_y = e \begin{pmatrix} 2\zeta_{1/2}k_y & \alpha_{R,1/2} & 0 & -\mathrm{i}\gamma \\ \alpha_{R,1/2} & 2\zeta_{1/2}k_y & \mathrm{i}\gamma & 0 \\ 0 & -\mathrm{i}\gamma & -2\zeta_{3/2}k_y & 0 \\ \mathrm{i}\gamma & 0 & 0 & -2\zeta_{3/2}k_y \end{pmatrix}. \tag{6b}$$

It is straightforward to find the four eigenstates of Hamiltonian in the pristine state:

$$|\vec{k}; \nu, \eta\rangle = |J, j_z\rangle = \frac{e^{\mathrm{i}\nu\pi/2}}{\sqrt{N_i}} \begin{pmatrix} e^{\mathrm{i}\nu\pi/2} \mathcal{D}_\nu^\eta \\ \mathcal{D}_{\nu+2}^\eta \\ \mathcal{D}_\nu^{\eta+2} \\ e^{\mathrm{i}\nu\pi/2} \mathcal{D}_{\nu+2}^{\eta+2} \end{pmatrix}, \tag{7}$$

where $N_i = \sum_{\nu,\eta} |\mathcal{D}_\nu^\eta|^2$ is the normalization factor with $i = \{1, 2, 3, 4\}$ and $\mathcal{D} = \{\psi, \phi, \chi, \mu\}$.

Following these data, the pristine $\mathcal{J}_{\alpha\beta;\nu\nu'}^{\eta\eta'}(\vec{k})$ can also be calculated analytically:

$$\mathcal{J}_{xx;-1,+1}^{-1,-1}(\vec{k}) = \frac{e^2}{N_1 N_3} \big[2\zeta_{1/2}k_x \big(\psi_{+1}^{-1}\chi_{+1}^{-1} - \psi_{-1}^{-1}\chi_{-1}^{-1} \big)$$
$$- \alpha_{R,1/2} \big(\psi_{-1}^{-1}\chi_{+1}^{-1} - \psi_{+1}^{-1}\chi_{-1}^{-1} \big)$$
$$+ \gamma \big(\psi_{+1}^{-1}\chi_{-1}^{+1} + \psi_{-1}^{+1}\chi_{+1}^{-1} - \psi_{-1}^{-1} - \chi_{-1}^{-1} \big) \big], \tag{8a}$$

$$\mathcal{J}_{xx;-1,+1}^{-1,+1}(\vec{k}) = \mathcal{J}_{xx;-1,+1}^{-1,-1}(\vec{k})|_{N_3 \mapsto N_4 \text{ and } \chi \mapsto \mu}, \tag{8b}$$

$$\mathcal{J}_{xx;-1,+1}^{+1,-1}(\vec{k}) = \mathcal{J}_{xx;-1,+1}^{-1,-1}(\vec{k})|_{N_1 \mapsto N_2 \text{ and } \chi \mapsto \phi}, \tag{8c}$$

$$\mathcal{J}_{xx;-1,+1}^{+1,+1}(\vec{k}) = \mathcal{J}_{xx;-1,+1}^{-1,-1}(\vec{k})|_{N_1 \mapsto N_2, N_3 \mapsto N_4 \text{ and } \psi \mapsto \phi, \chi \mapsto \mu}, \tag{8d}$$

with the following set of components for the eigenfunctions

$$\psi_{-1}^{-1} = \frac{-\alpha_{R,1/2}k - \tilde{\varepsilon} + \tilde{\zeta}k^2 - \mathcal{G}_{-1}(\vec{k})}{2\gamma k_+}, \tag{9a}$$

$$\psi_{+1}^{-1} = \frac{-\alpha_{R,1/2}k - \tilde{\varepsilon} - \tilde{\zeta}k^2 - \mathcal{G}_{-1}(\vec{k})}{2\gamma k}, \tag{9b}$$

$$\phi_{-1}^{-1} = \frac{-\alpha_{R,1/2}k - \tilde{\varepsilon} + \tilde{\zeta}k^2 + \mathcal{G}_{-1}(\vec{k})}{2\gamma k_+}, \tag{9c}$$

$$\phi_{+1}^{-1} = \frac{-\alpha_{R,1/2}k - \tilde{\varepsilon} - \tilde{\zeta}k^2 + \mathcal{G}_{-1}(\vec{k})}{2\gamma k}, \tag{9d}$$

$$\chi_{-1}^{-1} = \frac{+\alpha_{R,1/2}k - \tilde{\varepsilon} + \tilde{\zeta}k^2 - \mathcal{G}_{+1}(\vec{k})}{2\gamma k_+}, \tag{9e}$$

$$\chi_{+1}^{-1} = \frac{+\alpha_{R,1/2}k - \tilde{\varepsilon} - \tilde{\zeta}k^2 - \mathcal{G}_{+1}(\vec{k})}{2\gamma k}, \tag{9f}$$

$$\mu_{-1}^{-1} = \frac{+\alpha_{R,1/2}k - \tilde{\varepsilon} + \tilde{\zeta}k^2 + \mathcal{G}_{+1}(\vec{k})}{2\gamma k_+}, \tag{9g}$$

$$\mu_{+1}^{-1} = \frac{+\alpha_{R,1/2}k - \tilde{\varepsilon} - \tilde{\zeta}k^2 + \mathcal{G}_{+1}(\vec{k})}{2\gamma k}, \tag{9h}$$

where $\mathcal{G}_\nu(\vec{k})$ can be calculated from Eq. (2b). For all eigenstates, we have $\{\psi, \phi, \chi, \mu\}_{+1}^{+1} = 1$ and $\{\psi, \phi, \chi, \mu\}_{-1}^{+1} = k_-/k$.

Following the transformations $x \mapsto y$ and $k_x \mapsto k_y$, one can obtain the same equations along the y direction in the absence of CSB fields. On the other hand, for the Hall conductivity component, one needs to consider the multiplication of eignstates along different directions (not shown here). However, from Eq. (3), we also need to calculate the CSB field-induced eigenenergies and eigenstates. In contrast to the pristine case with full analytical expressions, for simplicity, we calculate the perturbed ones numerically and stress that the above transformations are not valid anymore as a direct consequence of CSB fields.

IV. PROPAGATION OF LIGHT IN MONOLAYER PBBII

In this section, we explore the properties of the reflected, transmitted, and absorbed light, i.e., the propagation of light, in the PbBiI monolayer based on the optical conductivity tensor. To start with, we assume that the PbBiI monolayer lies in the x-y plane, while the incident and scattered light propagate along the z direction. From the optics, it is well-known that the wave properties of incident, reflected, and transmitted light such as intensity and phase can be obtained from their corresponding complex electric fields $\vec{E}_i$, $\vec{E}_r = \underline{r}\vec{E}_i$, and $\vec{E}_t = \underline{t}\vec{E}_i$ at $z = 0$. In these relations, $\underline{r}$ and $\underline{t}$ are respectively 2×2 complex reflection and transmission matrices in the x-y plane.

For a right-circularly polarized light $\vec{E}_i = \frac{\mathcal{E}_0}{\sqrt{2}}(\vec{e}_x + i\vec{e}_y)$, the reflected and transmitted lights in the absence of CSB field are still circular, while they become elliptical as soon as the band structure is anisotropic due to the CSB field effect. Thus

we have [47]

$$\vec{E}_r = \frac{\mathcal{E}_0}{\sqrt{2}}(r_{xx}\vec{e}_x + i r_{yy}\vec{e}_y), \tag{10a}$$

$$\vec{E}_t = \frac{\mathcal{E}_0}{\sqrt{2}}(t_{xx}\vec{e}_x + i t_{yy}\vec{e}_y). \tag{10b}$$

If we ignore the effect of Pb-I dimer on the propagation of electric fields along the z direction, we find $r_{\alpha\alpha} = -4\pi\sigma_{\alpha\alpha}/[4\pi\sigma_{\alpha\alpha} + 2c]$ and $t_{\alpha\alpha} = 2c/[4\pi\sigma_{\alpha\alpha} + 2c]$ in which c is the speed of light [48,49].

Using the components of $r_{\alpha\alpha}$ and $t_{\alpha\alpha}$ along both x and y directions, the intensities of reflected, transmitted, and absorbed lights normalized to the incident intensity of light $I_{in} = \mathcal{E}_0^2$ read as

$$\frac{I_r(\omega)}{\mathcal{E}_0^2} = \frac{1}{2} \sum_\alpha \frac{|\sigma_{\alpha\alpha}(\omega)|^2}{(\frac{c}{2\pi} + \text{Re}\,\sigma_{\alpha\alpha}(\omega))^2 + (\text{Im}\,\sigma_{\alpha\alpha}(\omega))^2}, \tag{11a}$$

$$\frac{I_t(\omega)}{\mathcal{E}_0^2} = \frac{c^2}{8\pi^2} \sum_\alpha \frac{1}{\left(\frac{c}{2\pi} + \text{Re}\,\sigma_{\alpha\alpha}(\omega)\right)^2 + (\text{Im}\,\sigma_{\alpha\alpha}(\omega))^2}, \tag{11b}$$

$$\frac{I_{abs}(\omega)}{\mathcal{E}_0^2} = \frac{c}{2\pi} \sum_\alpha \frac{\text{Re}\,\sigma_{\alpha\alpha}(\omega)}{(\frac{c}{2\pi} + \text{Re}\,\sigma_{\alpha\alpha}(\omega))^2 + (\text{Im}\,\sigma_{\alpha\alpha}(\omega))^2}, \tag{11c}$$

which result in $I_r + I_t + I_{abs} = I_{in} = \mathcal{E}_0^2$ [47].

Having these information, we are also able to address the properties of polarization ellipse due to the anisotropic band structure of CSB-induced PbBiI. So, let us suppose that the general elliptically polarized wave is described by $\vec{E} = \frac{1}{2}([E_+ + E_-]\vec{e}_x + i[E_+ - E_-]\vec{e}_y)$ where $E_+ = \{r_{xx} - r_{yy}, t_{xx} - t_{yy}\}$ and $E_- = \{r_{xx} + r_{yy}, t_{xx} + t_{yy}\}$ [47]. The important property is the eccentricity given by

$$e_p^r = \frac{2}{\sqrt{\left|\frac{r_{xx} - r_{yy}}{r_{xx} + r_{yy}}\right|} + \sqrt{\left|\frac{r_{xx} + r_{yy}}{r_{xx} - r_{yy}}\right|}}, \tag{12a}$$

$$e_p^t = \frac{2}{\sqrt{\left|\frac{t_{xx} - t_{yy}}{t_{xx} + t_{yy}}\right|} + \sqrt{\left|\frac{t_{xx} + t_{yy}}{t_{xx} - t_{yy}}\right|}}, \tag{12b}$$

which both reflected and transmitted eccentricities are between 0 and 1 corresponding to the circularly and linearly polarized light, receptively. On the other hand, the scattered light is elliptically polarized for $0 < e_p^{r,t} < 1$.

V. NUMERICAL RESULTS AND DISCUSSION

As a first step before delving into the analysis of the results, we would stress that the arbitrary unit values in the present work for the optical conductivity will not affect the optical activity quantities. We restrict the thermal energy of the system to a very low value, $k_B T = 0.05$ eV, in an undoped ($\mu = 0$) situation. With these conditions, we assume that the momentum relaxation time approaches zero in the same bands at zero Fermi energy, which is mostly valid for a clean sample at a low temperature. This allows us to consider only the
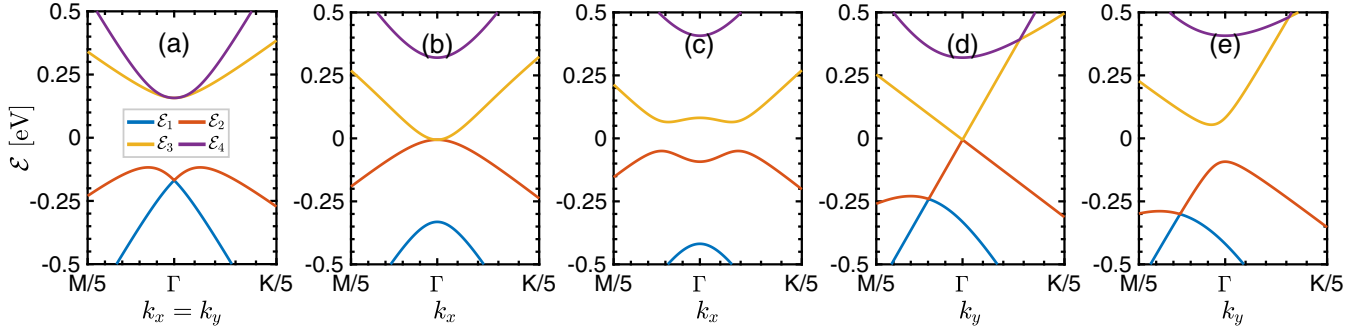
FIG. 2. Dispersion of monolayer PbBiI in the (a) absence and [(b)–(e)] presence of C_{3v} symmetry breaking field $\mathcal{F}_M = \{0.163, 0.25\}$ eV: [(b) and (c)] along the x direction and [(d) and (e)] along the y direction.

interband transitions and neglect the intraband ones in the next parts. It should be stressed that intraband transitions mainly contribute to the optical conductivity in the presence of the disorder or scattering in the THz region, which can be described as the Drude-like conductivity. This means that they mostly contribute to the peaks in the optical conductivity close to the zero photon energy. However, we do not consider any disorder or scattering mechanism in the theory for the optical transitions and with this, we are allowed to ignore the intraband transitions. On the other hand, for the Drude peaks, we will have the contribution of interband transitions. For this reason, we should argue that the modulation of intraband transitions is qualitatively close to the changes made for the interband transitions with the CSB fields.

The applied approximations throughout the model for a pedagogical aim allow us to work with qualitative (quantitative) results for the optical conductivities (intensities and eccentricities). In the pristine model with a valid approximation for the momenta so close to the Γ point, there is no priority for the propagation of light in the system due to the C_{3v} symmetry, and this, in turn, makes the conductivity strongly isotropic. This implies that although the first Brillouin zone of the system is a hexagonal, in order to work in the vicinity of Γ-point, we sum over $\vec{k}$ in the Kubo formula circularly, which leads to the isotropic optical conductivity. However, the CSB field makes it strongly anisotropic. In this work, we allow the light to enter the system with $\hbar\omega \leqslant 0.5$ eV because of the bandwidth of PbBiI, i.e., up to the near-infrared region of the electromagnetic spectrum. Also, it should be noted that all possible transitions at various $\vec{k}$ are scanned from the band structures in the summation over $\vec{k}$ in Eq. (4). However, the peaks corresponding to small currents at relative minimum/maximum points do not appear in the total optical conductivity and the contributions are mainly from the other points.

In the following, we consider the CSB fields individually and together. For each case, we first show the results of electronic band structure along both x and y directions to understand the alteration of bulk and Rashba-like gaps. Second, we numerically present the behavior of optical conductivity tensor with CSB fields. Third, the effect of CSB fields on the intensity of reflected, transmitted, and absorbed light in the PbBiI monolayer is discussed. And, finally, the change

in the polarization of the incident light with CSB fields is investigated.

A. $\mathcal{F}_M$ effects

We remark that the band dispersion is the origin of the interband transitions and it is especially important as we investigate a range of different values for the $\mathcal{F}_M$. So, first, we compare the band structures in both directions in Fig. 2. An interesting behavior observed in Figs. 2(b) and 2(d) is that a gapless phase appears in the system at $\mathcal{F}_M = (\varepsilon_{1/2} + \varepsilon_{3/2})/2 = 0.163$ eV, independent of the direction. This means that at this critical value of the field the PbBiI monolayer is not a QSHI. Below and above this critical field, the band-touching does not occur like the pristine phase. However, for $\mathcal{F}_M = 0.25$ eV, the bands along the x direction, see Fig. 2(c), become almost symmetric in the valence and conduction sides, while achieving different velocities and effective masses along the y direction they hold up their behaviors as the pristine phase, see Fig. 2(e). This, in turn, means that the effect of $\mathcal{F}_M$ on the electrons contributing to the Rashba-like states along the y direction is not considerable and bands 1 and 2 always try to touch each other. This is somehow a meaningful description of spatial symmetry breaking.

The corresponding optical interband transitions of $\mathcal{F}_M$-dependent $\sigma_{\alpha\beta}(\omega)$ is plotted in Fig. 3 along different directions. As we discussed before, the electronic band structure of the PbBiI monolayer consists of four different bands $\{\mathcal{E}_1, \mathcal{E}_2, \mathcal{E}_3, \mathcal{E}_4\}$. The general setting to be investigated in the following involves the optical selection rules in Fig. 1 (right panel). To tackle this problem by means of the above bands, one can easily write all interband transitions $\mathcal{E}_1 \mapsto \mathcal{E}_3$, $\mathcal{E}_1 \mapsto \mathcal{E}_4$, $\mathcal{E}_2 \mapsto \mathcal{E}_3$, and $\mathcal{E}_2 \mapsto \mathcal{E}_4$. It is obvious that the two first ones in the absence of $\mathcal{F}_M$ are the same at the Γ point. Furthermore, the intraband transitions $\mathcal{E}_1 \mapsto \mathcal{E}_2$ and $\mathcal{E}_3 \mapsto \mathcal{E}_4$ are forbidden based on our approximations. The total optical conductivity tensor can be evaluated from Eq. (4) right away by measuring each contribution. Figure 3(a) shows the real part of the total optical conductivity (in arbitrary units) of the PbBiI monolayer along the x direction in the absence and presence of CSB field $\mathcal{F}_M$. We remark that conductivities corresponding to the transitions from band 1 to bands $\{3,4\}$ and 2 to 4 in the case of $\mathcal{F}_M = 0$ (see the black line) is the origin of large optical
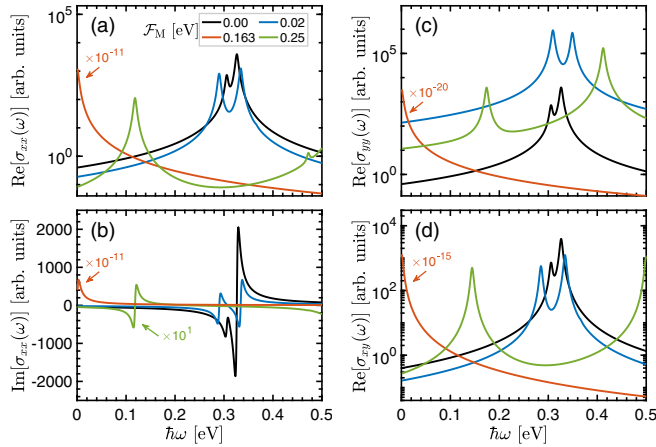
FIG. 3. A comparison between $\sigma_{\alpha\beta}(\omega)$ of monolayer PbBiI in the absence and presence of C_{3v} symmetry breaking field $\mathcal{F}_M$ [(a) and (b)] along the x direction, (c) along the y direction, and (d) in the x-y plane.

peak and it is especially important for the light frequency $\hbar\omega \simeq 0.326$ eV. The finite small peak of $\hbar\omega \simeq 0.3$ eV stems from the transition from band 2 to band 3. From these photon energies, one can argue that monolayer PbBiI is active in the region of near-infrared of electromagnetic spectrum. This ia also valid for other directions in the black lines of Figs. 3(c) and 3(d).

Therein, the optical peak positions are renormalized trivially with the external field and depend on the distance between bands in the electronic band structure. These peaks ensure that the band dispersion has the right modulation. We observe the insignificant of the $\mathcal{F}_M = 0.02$ eV-induced electron mode modulation along all directions: Specifically, we can see that the peaks are nearly shifted, satisfying the energy level repulsion effect, corresponding to the transitions between bands {2,3} and {2,4} along the x direction in Fig. 3(a) and in the x-y plane in Fig. 3(d), while between bands {1,3} and {1,4} along the y direction in Fig. 3(c), see the blue lines. At the critical field $\mathcal{F}_M = 0.163$ eV, the only interband transition between bands 2 and 3 is important. The gapless phase of the system leads to a large optical conductivity near the zero photon energy, referred to as a Drude peak [45,50]. The origin of this is lack of interband transition. In this case, at higher frequencies the spectrum deviates significantly from the Drude peak and drops down to zero as $1/\omega^2$.

Confronted with such a strong static response along all directions stemming from a single transition, we would immediately declare that for $\mathcal{F}_M = 0.25$ eV, different bands appear which directly manifest itself in the transitions such that bands {2,3} and {2,4} contribute to the x direction in the green line of Fig. 3(a), while bands {1,3} and {2,3} show corresponding peaks along the y direction and in the x-y plane in Figs. 3(c) and 3(d).

In a nutshell, it is worth noting that the system experiences an optical activity from the near-infrared to far-infrared region of the electromagnetic spectrum with the CSB field $\mathcal{F}_M$, which makes it applicable for many practical applications, especially those invisible to the human eye, from particle physics to universe physics. Independently of the CSB field effect, one
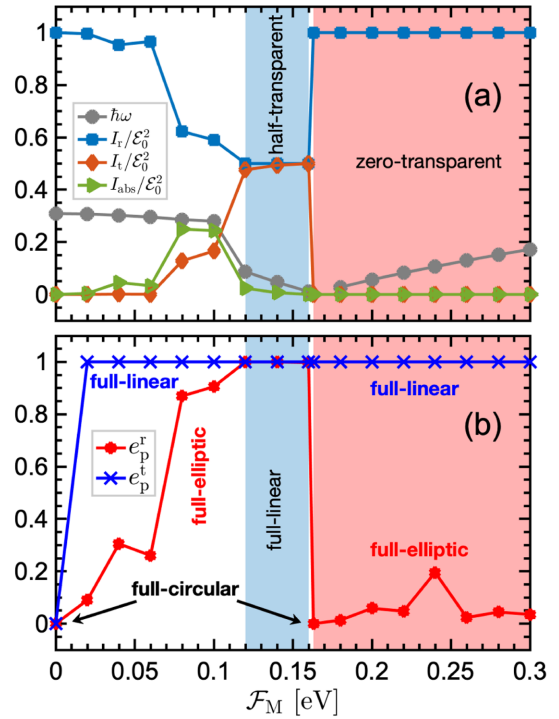

FIG. 4. (a) The relative intensity of reflected, transmitted, and absorbed light in monolayer PbBiI with respect to the incident light with intensity $\mathcal{E}_0^2$ as a function of CSB field $\mathcal{F}_M$. The photon energy $\hbar\omega$ of bright peak in the optical conductivity is also plotted vs. $\mathcal{F}_M$. (b) The reflected and transmitted eccentricities of monolayer PbBiI as a function of CSB field $\mathcal{F}_M$.

expects the same peak positions in the imaginary part of $\sigma_{\alpha\beta}(\omega)$ due to the Kramers-Kronig relation [51], see Fig. 3(b) for all CSB fields. For this reason, we mostly focus on the real part of optical conductivity tensor.

So far, we have discussed the optical conductivity of the system when it is subjected to a CSB field $\mathcal{F}_M$. Now, we proceed with the findings of optical activity in Fig. 4, characterized by Eqs. (11) and (12). First of all, the photon energy of bright peak in the optical conductivity is linearly changed with $\mathcal{F}_M < 0.1$ eV and suppressed strongly for $0.1 < \mathcal{F}_M < 0.12$ eV, see Fig. 4(a). For $0.12 \leqslant \mathcal{F}_M < 0.163$ eV, the static bright peaks (the Drude peaks) appear characterized by the zero photon energy. And above the critical field $\mathcal{F}_M = 0.163$ eV, the photon energy again becomes increasingly linear. These energies show interesting physical insights. As soon as the CSM field is in the region of $0.12 \leqslant \mathcal{F}_M < 0.163$ eV, static phase, the system is half-transparent such that the reflected and transmitted intensities are both equal to 0.5, while the absorbed light is almost zero. However, the system is not transparent at all for fields above 0.163 eV since the light is fully reflected and transmitted, whereas the absorbed spectrum approaches zero.

In addition to this information which is very handful for the optoelectronic devices, we can also provide some information about the light polarization in Fig. 4(b). For $0.01 < \mathcal{F}_M < 0.12$ eV, the polarization of the reflected (transmitted) light becomes fully elliptic (linear), while both become fully linear for $0.12 < \mathcal{F}_M < 0.16$ eV. At the critical CSB field of
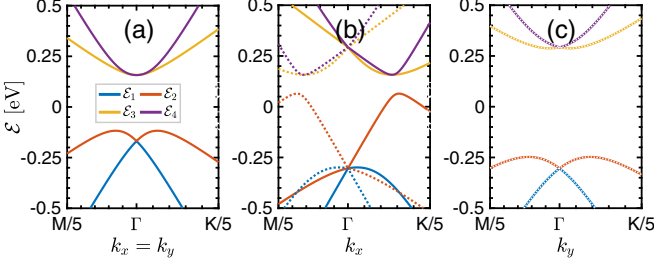
FIG. 5. Dispersion of monolayer PbBiI along both directions in the (a) absence and [(b) and (c)] presence of C_{3v} symmetry breaking field $\mathcal{F}_{\mathrm{ISB}} = 0.25$ eV. The dotted bands show the same results for $-\mathcal{F}_{\mathrm{ISB}}$.

$\mathcal{F}_{\mathrm{M}} = 0.163$ eV, the propagating light in the material shows its initial circular polarization. However, after crossing the border, one again finds fully elliptic (linear) polarization for the reflected (transmitted) light. Thus the CSB field is remarkably able to engineer the incident circular near-infrared light in the monolayer PbBiI for various purposes.

B. $\mathcal{F}_{\mathrm{ISB}}$ effects

In the next scenario, we work with $\mathcal{F}_{\mathrm{ISB}}$ field. The band dispersion of the Hamiltonian of Eq. (3b) is plotted in Fig. 5. The dispersion changes very strongly for a strong CSB field and it is only invariant under the operation $\mathcal{F}_{\mathrm{ISB}} \to -\mathcal{F}_{\mathrm{ISB}}$ (characterized by the dotted lines) along the y direction, meaning that there is no mirror symmetry around the Γ point, while it is the case along the x direction. As seen in Figs. 5(b) and 5(c), band touching of valence and conduction sides is independent of $\mathcal{F}_{\mathrm{ISB}}$ along both directions, in contrast to the previous CSB field in Fig. 2. While both gaps change strongly with $\mathcal{F}_{\mathrm{ISB}}$, interestingly, the bulk gap in the band structure along the y direction only becomes larger and the Rashba-like gap remains unchanged.

In Fig. 6, $\mathcal{F}_{\mathrm{ISB}}$-dependent optical conductivity for a variety of current direction are plotted. Similar to the previous CSB field $\mathcal{F}_{\mathrm{M}}$, the redshift and blueshift phenomena always occur for finite $\mathcal{F}_{\mathrm{ISB}}$s independent of the current direction. The value $\mathcal{F}_{\mathrm{ISB}} = 0.05$ eV shows a single optical peak along the x direction and in the x-y plane of monolayer PbBiI that is almost located at the optical energy $\hbar\omega \simeq 0.34$ eV corresponding to the interband transitions $\mathcal{E}_1 \mapsto \mathcal{E}_{3/4}$. However, in addition to the role of above transitions, the transition from band 2 to band 4 is also contributed to this large peak along the y direction, however, it appears along with a tiny peak at $\hbar\omega \simeq 0.32$ eV because of the interband transitions $\mathcal{E}_2 \mapsto \mathcal{E}_3$. For $\mathcal{F}_{\mathrm{ISB}} = 0.15$ eV, two peaks at $\hbar\omega \simeq 0.3$ and 0.44 eV appear along the x direction and in the x-y plane corresponding to, respectively, the transitions from bands 1 to {3,4} and 2 to 4, while we have a single peak for interband transitions $\mathcal{E}_1 \mapsto \mathcal{E}_{3/4}$ along the y direction. A stronger field of $\mathcal{F}_{\mathrm{ISB}} = 0.25$ eV investigated in the electronic band structure contributes differently to the optical selection rules in such a way that no peak appears along the y direction but two peaks appear in the optical conductivities of x direction and the x-y plane. In contrast to two other strengths of CSB field with the same treatments, the contribution of $\mathcal{E}_2 \mapsto \mathcal{E}_3$ ($\mathcal{E}_2 \mapsto \mathcal{E}_4$) and
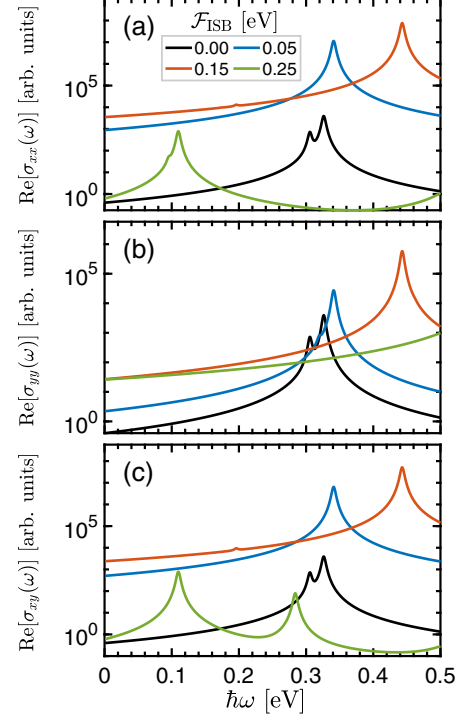

FIG. 6. A comparison between optical conductivity of monolayer PbBiI in the absence and presence of C_{3v} symmetry breaking field $\mathcal{F}_{\mathrm{ISB}}$ (a) along the x direction, (b) along the y direction, and (c) in the x-y plane.

$\mathcal{E}_2 \mapsto \mathcal{E}_4$ ($\mathcal{E}_2 \mapsto \mathcal{E}_3$) is responsible for the first (second) peak of x direction and the x-y plane, respectively. Various types of transitions confirm the C_{3v} symmetry breaking effect through $\mathcal{F}_{\mathrm{ISB}}$.

Despite the different optical peaks in the presence of $\mathcal{F}_{\mathrm{ISB}}$s compared to $\mathcal{F}_{\mathrm{M}}$s for various probing optical frequencies, similar elongation patterns can be observed far from the shifted intensities of reflected, transmitted, and absorbed lights. Let us compare these intensities for four CSB fields, namely $\mathcal{F}_{\mathrm{ISB}} = 0.08$, 0.163, 0.24, and 0.30 eV in Table I. It is demonstrated that, in general, the optical energy $\hbar\omega$ of bright peak moves toward higher frequencies with $\mathcal{F}_{\mathrm{ISB}}$. The reflected (transmitted and absorbed) spectrum is 1 (0) for fields below $(\varepsilon_{1/2} + \varepsilon_{3/2})/2 = 0.163$ eV, meaning that

TABLE I. A comparison between the relative intensity of reflected, transmitted, and absorbed light in monolayer PbBiI with respect to the incident light with intensity $\mathcal{E}_0^2$ for various CSB fields $\mathcal{F}_{\mathrm{ISB}}$. The photon energy $\hbar\omega$ of bright peak in the optical conductivity is considered for these extractions. The reflected and transmitted eccentricities of monolayer PbBiI are also compared.

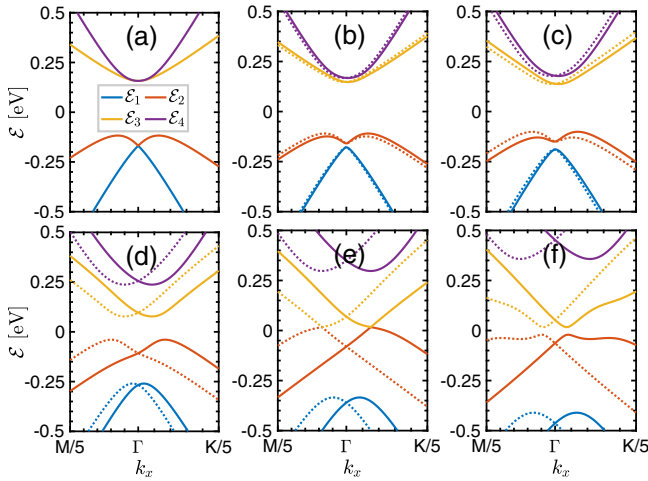| $\mathcal{F}_{\mathrm{ISB}}$	$\hbar\omega$	$I_{\mathrm{r}}/\mathcal{E}_0^2$	$I_{\mathrm{t}}/\mathcal{E}_0^2$	$I_{\mathrm{abs}}/\mathcal{E}_0^2$	$e_{\mathrm{p}}^{\mathrm{r}}$	$e_{\mathrm{p}}^{\mathrm{t}}$
0	0.3088	1	0	0	0	0
0.080	0.3394	1	0	0	0.0044	1
0.163	0.4294	1	0	0	0.0022	1
0.240	0.4234	0.7874	0.0293	0.1833	0.6521	1
0.300	0.4987	0.6394	0.1118	0.2488	0.8496	1

FIG. 7. Dispersion of monolayer PbBiI along the x direction in the (a) absence and [(b)–(f)] presence of C_{3v} symmetry breaking field $\mathcal{F}$: (b) 0.01, (c) 0.02, (d) 0.08, (e) 0.14, and (f) 0.20 eV.

FIG. 8. Dispersion of monolayer PbBiI along the y direction in the (a) absence and [(b)–(f)] presence of C_{3v} symmetry breaking field $\mathcal{F}$: (b) 0.05, (c) 0.10, (d) 0.20, (e) 0.35, and (f) 0.50 eV.

the system is not transparent at all. At the same time, the polarization of reflected (transmitted) light remains almost circular (becomes fully linear). Above the field 0.163 eV, at $\mathcal{F}_{ISB} = 0.24$ eV, the incident light is strongly scattered such that around 79% is reflected from the monolayer PbBiI, 18% is absorbed in the system, and 3% is transmitted. For $\mathcal{F}_{ISB} = 0.3$ eV, however, the percentages are different: We have almost 64% reflection, 11% transmission, and 25% absorption. The polarization of scattered lights are, respectively, fully elliptic and fully linear for the reflected and transmitted ones.

C. $\mathcal{F}$ effects

In the last scenario, we work with both fields compacted in $\mathcal{F}$ in Eq. (3c). Let us start with the x direction in Fig. 7. As soon as the CSB field is turned on with a magnetization induced from the ferromagnetic substrate in parallel to the spin up $j_z = +1/2$ (solid lines), the Rashba-like gap is disappeared, first. Second, subsequently, two different behaviors can be distinguished for the bulk gap depending on the critical field $|\mathcal{F}_c| = 0.14$ eV as illustrated in Fig. 7(e). The predicted critical field is due to the competition between the bulk gap and CSB field, i.e., $|\mathcal{F}_c| \simeq (\mathcal{E}_3 - \mathcal{E}_2)/2$. Below and above this critical field, the bulk gap is open, while at this field it is closed, meaning that the system transits to a new gapless phase and is no longer a QSHI. If we set the direction of the magnetization parallel to the spin down $j_z = -1/2$ (dotted lines), the same behaviors emerge with a mirror symmetry property around the Γ point without any new physical implications.

Following the same procedure presented above and having new band dispersion as a direct result of $\mathcal{F}$, we plot the electronic band structure of the system along the y direction in Fig. 8 to see if different physical insights can be achieved. First of all, in contrast to the x direction, stronger fields are required to achieve a gapless state along the y direction such that our numerical tests need at least 25 eV energy to close the bulk gap which is of course unphysical because in that case,
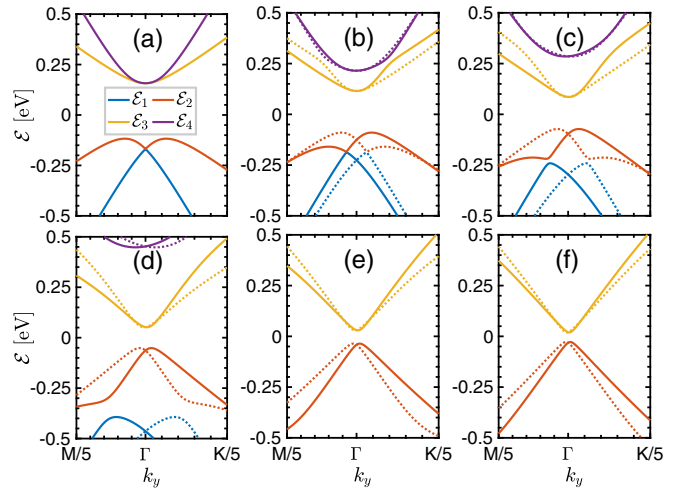
our low-energy Hamiltonian is not valid anymore. So, we do not argue a phase transition along the y direction with the same CSB fields as the x direction. However, for other fields which can also be applied along the x direction, we obviously find the disappearance of Rashba-like gap. Simultaneously, the bulk gap is reduced as the CSB field is increased. These changes will also be important in the optical properties of the system.

The corresponding optical results for the impact of $\mathcal{F}$ are shown in Fig. 9(a). Let us provide an effective optical selection rule along the x direction from Fig. 7. For $0 < \mathcal{F} < 0.14$ eV, we expect all transitions to appear effectively in the optical conductivity. For $\mathcal{F} = 0.01$ eV, we observe three peaks (two large and one small), respectively from low to high optical energies, corresponding to the transition from band $2 \mapsto 3$, $\{1 \mapsto 3$ and $2 \mapsto 4\}$, and $1 \mapsto 4$. For $\mathcal{F} = \{0.02, 0.08\}$ eV, four peaks (the last one in the case of 0.08 eV locates at $\hbar\omega \simeq$
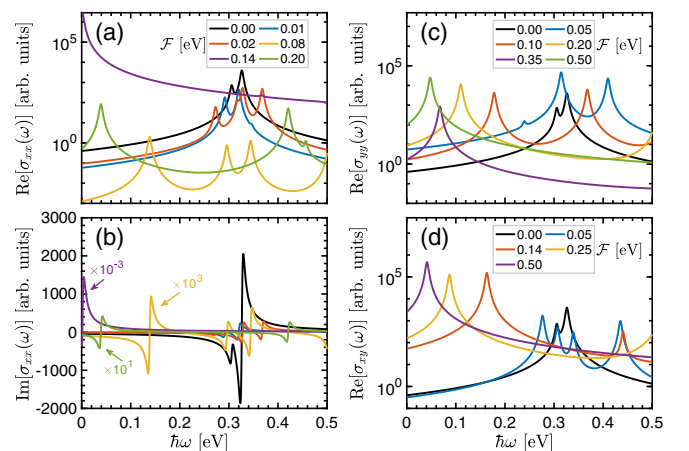

FIG. 9. A comparison between the absence and presence of CSB field $\mathcal{F}$ in the (a) real and (b) imaginary parts of optical conductivity of monolayer PbBiI along the x direction through behaviors of peaks. The real part of optical conductivity along the y direction and in the x-y plane are presented in (c) and (d), respectively.
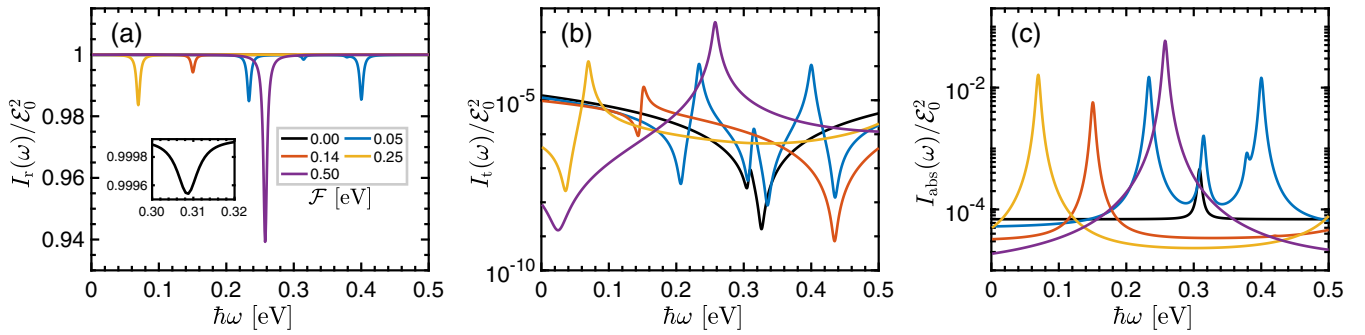
FIG. 10. The relative intensity of (a) reflected, (b) transmitted, and (c) absorbed light with respect to the incident light with intensity $\mathcal{E}_0^2$ for different CSB fields $\mathcal{F}$ as a function of photon energy $\hbar\omega$.

0.5 eV) appear, respectively, corresponding to the transitions $2 \mapsto 3$, $2 \mapsto 4$, $1 \mapsto 3$, and $1 \mapsto 4$. The position of these peaks is in agreement with the distance between corresponding bands in Figs. 7(b)–7(d). Therein, the peak positions are renormalized with CSB field and their intensity strongly depend on the distance of bands from the Γ point [see the denominator of Eq. (3)] such that for $\mathcal{F} = 0.08$ eV, the height of peak is small compared to two other cases $\mathcal{F} = 0.01$ and 0.02 eV.

For $\mathcal{F} = 0.14$ eV, as discussed before, the bulk gap is closed and the Rashba-like gap is disappeared. The system in this gapless phase is also confronted with a tiny peak at $\hbar\omega \simeq 0.36$ eV corresponding to the transition between bands 1 and 3 in Fig. 7(e). Its intensity is too small since the bands are far from the Γ point. Despite the behaviors of CSB fields below 0.14 eV, for $\mathcal{F} > 0.14$ eV, the bands become closer to the Γ point and the intensity of optical peaks are again visible, see the green line of Fig. 9(a) at $\hbar\omega \simeq \{0.04, 0.42, \text{and } 0.46\}$ eV corresponding to the distance between bands $\{2,3\}$, $\{2,4\}$, and $\{1,3\}$ in Fig. 7(f). The transition between bands 1 and 4 is negligible for $\mathcal{F} = 0.2$ eV.

Let us only concentrate on the real part of optical conductivity in Fig. 9 for other components yy and xy by leaving the imaginary part following the Kramers-Kronig relation. As expected, in the pristine model, the conductivity is isotropic, namely $\sigma_{xx} = \sigma_{yy} = \sigma_{xy}$, as confirmed by the black lines in Figs. 9(a), 9(c), and 9(d). The most evident result of this figure is the close intensities of responses at nonzero $\mathcal{F}$ to the pristine response due to small distance of bands along the y direction from the Γ point, see Fig. 8, in a complete agreement with the argument mentioned before. Next, we strive to find the optical peaks corresponding to the transition between bands by evaluating the CSB field-induced $\sigma_{yy}(\omega)$ and $\sigma_{xy}(\omega)$ from Eq. (4). To do this, we consider $\mathcal{F} = 0.05$, 0.10, 0.20, 0.35, and 0.50 eV along the y direction and $\mathcal{F} = 0.05$, 0.14, 0.25, and 0.50 in the x-y plane. Then, we plug their corresponding transitions into these conductivities. For $\mathcal{F} = 0.05$ eV, the band structure along the y direction, see Fig. 8(b), still contains the Rashba-like splitting gap and the transition from band 2 to 4 is negligible. For this reason, the blue line in $\sigma_{yy}(\omega)$ shows three peaks: Two large and one small from the transitions $2 \mapsto 3$, $1 \mapsto 3$, and $1 \mapsto 4$, respectively. The results show that optical responses for $0.05 < \mathcal{F} < 0.20$ eV appear with two peaks and move to the lower photon energies if we increase the field further, originating from the transitions $2 \mapsto 3$ and $\{1 \mapsto 3$ and $2 \mapsto 4\}$, see Figs. 8(c)–8(f). Similar

to the x direction, the y direction of the system undergoes a near-infrared to far-infrared shift with $\mathcal{F}$. For $\mathcal{F} > 0.20$ eV, we only have a single peak from the bands 2 and 3 as the effective ones.

At $\mathcal{F} = 0.05$ eV, the x direction contains all the transitions, while the y direction does not contain the transition between bands 2 and 4 (negligible). However, for the transitions in the x-y plane, we again have all four transitions and that's why four peaks appear in the blue line of Fig. 9(d). The peaks originate, respectively, from $2 \mapsto 3$, $2 \mapsto 4$, $1 \mapsto 3$, and $2 \mapsto 4$. For $\mathcal{F} = 0.14$ eV, we observe two peaks from the transitions $2 \mapsto 3$ and $1 \mapsto 3$. Again, the position of peaks are equal to the distance between these bands (a three-dimensional band structure is needed here to confirm it, which is not shown here). Although for $\mathcal{F} = 0.05$ eV, we observe close intensities to the pristine peaks for the Hall conductivity, $\mathcal{F} = 0.14$ eV demonstrates a higher intensity. The main reason for this behavior can be traced back to the gapless phase of the system at this field along the x direction for which the optical conductivity appeared with the highest intensities over a wide range of infrared photon energies. Nevertheless, it is obvious that the y direction neutralizes the Drude peak effect in the x-y plane. For $\mathcal{F} > 0.14$ eV, a single Hall peak from the transition $2 \mapsto 3$ appears for all CSB fields in the x-y plane. Moreover, the near-infrared to far-infrared shift with $\mathcal{F}$ is also valid in the x-y plane.

Next, we aim at achieving a quantitative understanding of $\mathcal{F}$ effect on the intensity of reflected, transmitted, and absorbed light, Eqs. (11a)–(11c), in Fig. 10. This figure shows that the reflection is almost 100% for frequencies below and above 0.3 eV when the C_{3v} symmetry is not broken and this energy just leads to almost 99.995% reflection, 0% transmission, and 0.005% absorption inherently. So, the system is not intrinsically transparent. Nevertheless, by turning on the CSB field which results in the band dispersion modulation along both directions, at $\mathcal{F} = 0.05$ eV from the blue lines of all three panels, the reflection is suppressed by 1.5%, the transmission is still close to zero, and the absorption is increased by 1.5% to satisfy the standard sum rule $I_r + I_t + I_{abs} = \mathcal{E}_0^2$. At $\mathcal{F} = 0.14$ eV from the red lines, only 0.5% is obtained for both reflection and absorption spectra. For $\mathcal{F} = 0.25$ eV from the dark yellow lines, 1.7% alteration for both reflection and absorption is obtained. However, for $\mathcal{F} = 0.5$ eV from the magenta lines, 4% reflection and absorption can be achieved. In all cases, the contribution of transmission spectra is negli-
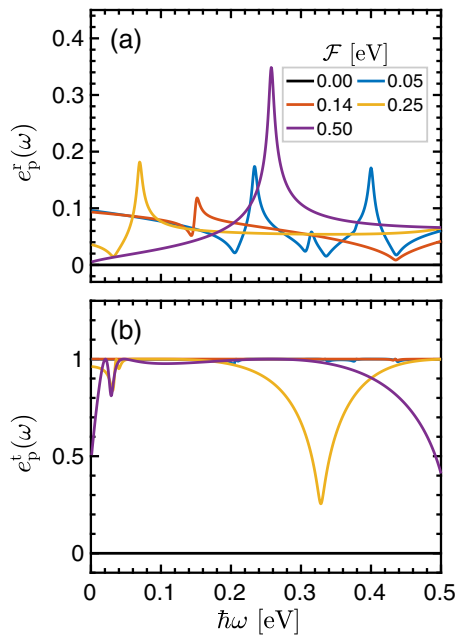
FIG. 11. Eccentricity of the (a) reflected and (b) transmitted electromagnetic wave as a function of the photon energy for different CSB fields $\mathcal{F}$.

gible in the sum rule, thus, PbBiI does not become transparent with $\mathcal{F}$.

In the following, we would like to address the effect of $\mathcal{F}$ field on the eccentricity of scattered lights to see if our argument about the circularly-to-elliptically polarized transition is valid. Figure 11 shows the behavior of the parameters e_p^r and e_p^t defined in Eqs. (12a) and (12b) for the reflected and transmitted components, respectively. As mentioned before, when applying a circularly polarized light to the plane of the material, anisotropy in the optical conductivity due to the CSB field forms elliptically scattered waves. As indicated in Fig. 11, both reflected and transmitted indicate zero eccentricities in the absence of $\mathcal{F}$. As soon as we turn on the CSB field, the reflected light is strongly elliptic in a wide range of photon energies for all finite CSB fields. Interestingly, the transmitted light reaches a linear polarization for $\mathcal{F} \leqslant 0.14$ eV, except that it becomes elliptic at special photon frequencies corresponding to the peak positions of transmission intensity. For $\mathcal{F} > 0.14$ eV, however, the transmitted light is more interested in reaching the elliptical polarization. It seems that transmitted light even intends to go back to the circular polarization at some energies depending on the CSB field.

Before scrutinizing the consequences of the CSB field on the optical conductivity and activity of monolayer PbBiI, we finish our discussion by briefly commenting on the doping effect. For our intention to relate the behavior of the system to the doping effect, it should be stressed that our results are valid for a low-energy approximation model, and the finite Fermi energy shifts the bands up and down depending on the electron or hole doping configuration. By this, the selection rules, optical transitions, and the position of peaks in the optical properties can not be influenced. Therefore the qualitative behavior of responses remains unchanged with doping process.

The model presented here treats the CSB-dependent electronic and optical properties well, and this makes various applications possible. For example, in biological effects, materials with far-infrared wavebands are nowadays used to stimulate cells and tissues [52]. Also, they can be generated in the depletion field near semiconductor surfaces under optical excitation [53]. In the study of extrasolar planets as well as photonic applications, the feasibility of infrared optical fibers formed from the far-infrared-active materials is recommended [54,55].

VI. CONCLUSIONS

Interests in exploring the physics of topological systems in the experimental photonic and spintronic setups are becoming increasingly urgent. This paper studies the propagation of light engineering in a noncentrosymmetric quantum spin hall insulator, monolayer PbBiI, which dealt with special C_{3v} symmetry breaking fields accompanying the effects of anisotropic band dispersion on the optical responses. Two ways are possible to show that the system is near-infrared active. The first way is focused on the spectrum of optical conductivity through the Kubo formula. While the second way is the optical activity of the system stars the intensity of reflected, transmitted, and absorbed light.

In the spirit of a $\vec{k} \cdot \vec{p}$ model, we calculated these quantities. In particular, we have focused on the effects of special fields to explore novel insights by examination of the band dispersion that makes up the contribution to the optical interband transitions. Detailed analyses showed that the optical responses of the system reach various activity transitions from near-infrared to far-infrared with C_{3v} symmetry breaking fields. Notably, we also observed that, depending on the strength of fields in the PbBiI single layer, the incident circularly polarized light is scattered as various linearly and elliptically polarized light. These results are important for a wide range of applications in science, industry, and medicine.

[1] K. V. Klitzing, G. Dorda, and M. Pepper, New Method for High-Accuracy Determination of the Fine-Structure Constant Based on Quantized Hall Resistance, Phys. Rev. Lett. **45**, 494 (1980).

[2] K. von Klitzing, The quantized hall effect, Rev. Mod. Phys. **58**, 519 (1986).

[3] K. S. Novoselov, D. Jiang, F. Schedin, T. J. Booth, V. V. Khotkevich, S. V. Morozov, and A. K. Geim, Two-dimensional atomic crystals, Proc. Natl. Acad. Sci. USA **102**, 10451 (2005).

[4] K. S. Novoselov, A. K. Geim, S. V. Morozov, D. Jiang, Y. Zhang, S. V. Dubonos, I. V. Grigorieva, and A. A. Firsov,

Electric field effect in atomically thin carbon films, Science **306**, 666 (2004).

[5] K. S. Novoselov, Nobel lecture: Graphene: Materials in the flatland, Rev. Mod. Phys. **83**, 837 (2011).

[6] C. L. Kane and E. J. Mele, Quantum Spin Hall Effect in Graphene, Phys. Rev. Lett. **95**, 226801 (2005).

[7] B. A. Bernevig, T. L. Hughes, and S.-C. Zhang, Quantum spin hall effect and topological phase transition in hgte quantum wells, Science **314**, 1757 (2006).

[8] M. König, S. Wiedmann, C. Brüne, A. Roth, H. Buhmann, L. W. Molenkamp, X.-L. Qi, and S.-C. Zhang, Quantum spin hall insulator state in hgte quantum wells, Science **318**, 766 (2007).

[9] L. Kou, Y. Ma, Z. Sun, T. Heine, and C. Chen, Two-dimensional topological insulators: Progress and prospects, J. Phys. Chem. Lett. **8**, 1905 (2017).

[10] M. Z. Hasan and C. L. Kane, Colloquium: Topological insulators, Rev. Mod. Phys. **82**, 3045 (2010).

[11] X.-L. Qi and S.-C. Zhang, Topological insulators and superconductors, Rev. Mod. Phys. **83**, 1057 (2011).

[12] B. Yan and S.-C. Zhang, Topological materials, Rep. Prog. Phys. **75**, 096501 (2012).

[13] S. Maekawa, S. O. Valenzuela, E. Saitoh, and T. Kimura, *Spin Current*, Series on Semiconductor Science and Technology (OUP Oxford, 2012).

[14] A. Manchon, H. C. Koo, J. Nitta, S. M. Frolov, and R. A. Duine, New perspectives for rashba spin–orbit coupling, Nat. Mater. **14**, 871 (2015).

[15] D. Bercioux and P. Lucignano, Quantum transport in rashba spin–orbit materials: A review, Rep. Prog. Phys. **78**, 106001 (2015).

[16] J. Nitta, T. Akazaki, H. Takayanagi, and T. Enoki, Gate control of spin-orbit interaction in an inverted $in_{0.53}ga_{0.47}as/in_{0.52}al_{0.48}as$ heterostructure, Phys. Rev. Lett. **78**, 1335 (1997).

[17] T. Hirahara, T. Nagao, I. Matsuda, G. Bihlmayer, E. V. Chulkov, Yu. M. Koroteev, P. M. Echenique, M. Saito, and S. Hasegawa, Role of Spin-Orbit Coupling and Hybridization Effects in the Electronic Structure of Ultrathin Bi Films, Phys. Rev. Lett. **97**, 146803 (2006).

[18] S. Mathias, A. Ruffing, F. Deicke, M. Wiesenmayer, I. Sakar, G. Bihlmayer, E. V. Chulkov, Yu. M. Koroteev, P. M. Echenique, M. Bauer, and M. Aeschlimann, Quantum-Well-Induced Giant Spin-Orbit Splitting, Phys. Rev. Lett. **104**, 066802 (2010).

[19] H. Yuan, M. S. Bahramy, K. Morimoto, S. Wu, K. Nomura, B.-J. Yang, H. Shimotani, R. Suzuki, M. Toh, C. Kloc, X. Xu, R. Arita, N. Nagaosa, and Y. Iwasa, Zeeman-type spin splitting controlled by an electric field, Nat. Phys. **9**, 563 (2013).

[20] J. H. Dil, F. Meier, J. Lobo-Checa, L. Patthey, G. Bihlmayer, and J. Osterwalder, Rashba-Type Spin-Orbit Splitting of Quantum Well States in Ultrathin Pb Films, Phys. Rev. Lett. **101**, 266802 (2008).

[21] C. Mera Acosta, O. Babilonia, L. Abdalla, and A. Fazzio, Unconventional spin texture in a noncentrosymmetric quantum spin hall insulator, Phys. Rev. B **94**, 041302(R) (2016).

[22] A. Ström, H. Johannesson, and G. I. Japaridze, Edge Dynamics in a Quantum Spin Hall State: Effects from Rashba Spin-Orbit Interaction, Phys. Rev. Lett. **104**, 256804 (2010).

[23] J. C. Budich, F. Dolcini, P. Recher, and B. Trauzettel, Phonon-Induced Backscattering in Helical Edge States, Phys. Rev. Lett. **108**, 086602 (2012).

[24] F.çois Crépin, J. C. Budich, F. Dolcini, P. Recher, and B. Trauzettel, Renormalization group approach for the scattering off a single rashba impurity in a helical liquid, Phys. Rev. B **86**, 121106(R) (2012).

[25] T. L. Schmidt, S. Rachel, F. von Oppen, and L. I. Glazman, Inelastic Electron Backscattering in a Generic Helical Edge Channel, Phys. Rev. Lett. **108**, 156402 (2012).

[26] J. I. Väyrynen, M. Goldstein, and L. I. Glazman, Helical Edge Resistance Introduced by Charge Puddles, Phys. Rev. Lett. **110**, 216402 (2013).

[27] F. Geissler, F. Crépin, and B. Trauzettel, Random rashba spin-orbit coupling at the quantum spin hall edge, Phys. Rev. B **89**, 235136 (2014).

[28] K. Jiang, S. Zhou, X. Dai, and Z. Wang, Antiferromagnetic Chern Insulators in Noncentrosymmetric Systems, Phys. Rev. Lett. **120**, 157205 (2018).

[29] T. C. Phong, V. T. Lam, and B. D. Hoi, Tuning electronic phase in noncentrosymmetric quantum spin Hall insulators through physical stimuli, J. Phys.: Condens. Matter **33**, 325502 (2021).

[30] L. T. T. Phuong, T. C. Phong, B. D. Hoi, and M. Yarmohammadi, Enhancement of the thermoelectric power factor in monolayer PbBiI: staggered exchange field effect, J. Mater. Chem. A **10**, 16620 (2022).

[31] M. König, H. Buhmann, L. W. Molenkamp, T. Hughes, C.-X. Liu, X.-L. Qi, and S.-C. Zhang, The quantum spin hall effect: Theory and experiment, J. Phys. Soc. Jpn. **77**, 031007 (2008).

[32] B. Scharf, A. Matos-Abiague, and J. Fabian, Magnetic properties of hgte quantum wells, Phys. Rev. B **86**, 075418 (2012).

[33] P. Debray, S. M. S. Rahman, J. Wan, R. S. Newrock, M. Cahay, A. T. Ngo, S. E. Ulloa, S. T. Herbert, M. Muhammad, and M. Johnson, All-electric quantum point contact spin-polarizer, Nat. Nanotechnol. **4**, 759 (2009).

[34] P. Chuang, S.-C. Ho, L. W. Smith, F. Sfigakis, M. Pepper, C.-H. Chen, J.-C. Fan, J. P. Griffiths, I. Farrer, H. E. Beere, G. A. C. Jones, D. A. Ritchie, and T.-M. Chen, All-electric all-semiconductor spin field-effect transistors, Nat. Nanotechnol. **10**, 35 (2015).

[35] A. T. Ngo, P. Debray, and S. E. Ulloa, Lateral spin-orbit interaction and spin polarization in quantum point contacts, Phys. Rev. B **81**, 115328 (2010).

[36] N. A. Gokcen, The bi-pb (bismuth-lead) system, J. Phase Equilib. **13**, 21 (1992).

[37] H.-C. W. Huang and C. M. Serrano, Preparation of Pb-Bi film by alloy evaporation ii. microstructure and morphology, J. Vac. Sci. Technol. A **1**, 1409 (1983).

[38] I. K. Drozdov, A. Alexandradinata, S. Jeon, S. Nadj-Perge, H. Ji, R. J. Cava, B. Andrei Bernevig, and A. Yazdani, One-dimensional topological edge states of bismuth bilayers, Nat. Phys. **10**, 664 (2014).

[39] R. Yu, X. L. Qi, A. Bernevig, Z. Fang, and X. Dai, Equivalent expression of z_2 topological invariant for band insulators using the non-abelian berry connection, Phys. Rev. B **84**, 075119 (2011).

[40] A. A. Soluyanov and D. Vanderbilt, Wannier representation of z_2 topological insulators, Phys. Rev. B **83**, 035108 (2011).

[41] A. A. Soluyanov and D. Vanderbilt, Computing topological invariants without inversion symmetry, Phys. Rev. B **83**, 235401 (2011).

[42] A. Ullah and K. Sabeeh, Optical conductivity of topological insulator thin films in a quantizing magnetic field, J. Phys.: Condens. Matter **26**, 505303 (2014).

[43] Q.-Q. Zhang, Q. Li, X.-T. An, and J.-J. Liu, Valley-resolved quantum anomalous hall effect in ferromagnetically proximitized monolayer mote$_2$, Phys. Rev. B **105**, 205436 (2022).

[44] M. Bora and P. Deb, Magnetic proximity effect in two-dimensional van der waals heterostructure, J. Phys. Mater. **4**, 034014 (2021).

[45] G. D. Mahan, *Many-Particle Physics*, Physics of Solids and Liquids (Springer US, New York, 2000).

[46] N. A. Sinitsyn, J. E. Hill, H. Min, J. Sinova, and A. H. MacDonald, Charge and Spin Hall Conductivity in Metallic Graphene, Phys. Rev. Lett. **97**, 106804 (2006).

[47] J. D. Jackson, *Classical Electrodynamics* (Wiley, New York, 1998).

[48] W.-K. Tse and A. H. MacDonald, Magneto-optical faraday and kerr effects in topological insulator films and in other layered quantized hall systems, Phys. Rev. B **84**, 205327 (2011).

[49] M. Lasia and L. Brey, Optical properties of magnetically doped ultrathin topological insulator slabs, Phys. Rev. B **90**, 075417 (2014).

[50] G. Grosso and G. P. Parravicini, *Solid State Physics* (Elsevier Science, Amsterdam 2013).

[51] R. de L. Kronig and H. A. Kramers, Zur theorie der absorption und dispersion in den röntgenspektren, Z. Phys. **48**, 174 (1928).

[52] F. Vatansever and M. R. Hamblin, Far infrared radiation (FIR): Its biological effects and medical applications, Photonics & Lasers in Medicine **1**, 255 (2012).

[53] B. I. Greene, P. N. Saeta, D. R. Dykaar, S. Schmitt-Rink, and S. L. Chuang, Far-infrared light generation at semiconductor surfaces and its spectroscopic applications, IEEE J. Quantum Electron. **28**, 2302 (1992).

[54] S. Danto, P. Houizot, C. Boussard-Pledel, X.-H. Zhang, F. Smektala, and J. Lucas, A family of far-infrared-transmitting glasses in the Ga-Ge-Te system for space applications, Adv. Funct. Mater. **16**, 1847 (2006).

[55] P. Lucas, Z. Yang, M. K. Fah, T. Luo, S. Jiang, C. Boussard-Pledel, M.-L. Anne, and B. Bureau, Telluride glasses for far infrared photonic applications, Opt. Mater. Express **3**, 1049 (2013).